Gallium Arsenide Photonic Integrated Circuit Platform for Tunable Laser Applications

Paul A. Verrinder, Lei Wang, Joseph Fridlander, Fengqiao Sang, Victoria Rosborough, Michael Nickerson, Guangning Yang, Mark Stephen, Larry Coldren, *Life Fellow, IEEE*, and Jonathan Klamkin, *Senior Member, IEEE*

***Abstract*—An active-passive integration technique for operation near a wavelength of 1030 nm has been developed on a gallium arsenide (GaAs) photonic integrated circuit platform. The technique leverages quantum wells (QWs) that are slightly offset vertically from the center of the waveguide, and selectively removed prior to upper cladding regrowth to form active and passive regions. The active region consists of indium gallium arsenide (InGaAs) QWs, gallium arsenide phosphide (GaAsP) barriers, GaAs separate confinement heterostructure layers, and aluminum gallium arsenide (AlGaAs) cladding. Fabry Perot lasers with various widths were fabricated and characterized, exhibiting high injection efficiency of 98.8%, internal active loss of 3.44 cm^{-1}, and internal passive loss of 4.05 cm^{-1} for 3 μm wide waveguides. The 3 μm, 4 μm, and 5 μm wide lasers demonstrated greater than 50 mW output power at 100 mA continuous wave (CW) current and threshold current as low as 9 mA. 20 μm wide broad area lasers demonstrated 240 mW output power, 35.2 mA threshold current under CW operation, and low threshold current density of 94 A/cm^2 for 2 mm long lasers. Additionally, these devices exhibit transparency current density of 85 A/cm^2 and good thermal characteristics with $T_0 = 205$ K, and $T_\eta = 577$K.**

***Index Terms*—InGaAs quantum well, LiDAR, photonic integrated circuits (PIC), quantum well lasers, semiconductor lasers, tunable laser.**

I. Introduction

Since their invention, semiconductor laser diodes have become ubiquitous as compact, highly efficient, coherent light sources for a wide variety of applications, particularly within the telecommunications industry. In continual pursuit of reduced cost, size, weight, and power (CSWaP), additional optical components such as modulators, optical amplifiers, and photodetectors have been monolithically integrated with laser light sources to generate photonic integrated circuits (PICs) [1], [2]. The primary application of PIC technology to date has been for optical data communications, where indium phosphide (InP) based platforms have achieved the highest level of integration in order to leverage the low-loss optical fiber spectral regions around 1310 nm and 1550 nm [1]–[3]. Building on the maturation of PIC technology, PICs have also been pursued for other applications including free space laser communications, microwave photonics, 3D mapping light detection and ranging (Lidar), and remote gas sensing Lidar [4]–[6]. Additionally, there are applications outside of the traditional optical communications wavelength regions that could benefit from the CSWaP reduction offered by PIC technology. The focus of this work is on development of a PIC platform operating with a wavelength near 1030 nm for use in Lidar, specifically for airborne and space applications where deployment on small platforms is highly desirable. Wavelengths such as 1030 nm or 1064 nm are common choices for topographical Lidar systems owing to low atmospheric absorption and the existence of high-quality detectors, such as silicon or indium gallium arsenide (InGaAs) avalanche photodiodes (APDs), for this spectral range [7], [8]. CSWaP is of critical importance for any airborne or space-based system, and PIC technology at this wavelength would allow for multiple optical components to be integrated onto a single compact platform, while still leveraging the advantages of this wavelength for Lidar and sensing.

Gallium arsenide (GaAs) lasers based on strained layer InGaAs/GaAs quantum wells (QWs) have been used to build efficient laser diodes with high power output near 1 μm for many years [9] and are an obvious choice for this application. However, to date most laser development in this wavelength regime has focused on high power Fabry Perot [10], [11], distributed Bragg reflector (DBR), and distributed feedback (DFB) laser diodes [12], [13]. These were constructed primarily with large optical cavities and thick waveguide layers making them unsuitable for the active-passive integration necessary for PICs. Little work has been pursued for integrating 1 μm lasers with other active and passive optical components on a compact PIC platform analogous to InP PICs, or to develop widely tunable lasers near 1030 nm. In this paper, we demonstrate an active-passive integration technique on GaAs, for operation near 1030 nm, to enable PICs with widely tunable lasers. We also present designs and development for widely tunable lasers with sampled grating DBR (SGDBR) mirrors for extended tuning range, and integrated semiconductor optical amplifiers (SOA). This work

Manuscript received April 7, 2021; revised May 24, 2021; accepted May 29, 2021. Date of publication June 2, 2021; date of current version July 16, 2021. This work was supported by the NASA ESTO Advance Component Technology program. A portion of this work was carried out in the UCSB Nanofabrication Facility. *(Corresponding author: Paul A. Verrinder.)*

Paul A. Verrinder, Lei Wang, Joseph Fridlander, Fengqiao Sang, Victoria Rosborough, Michael Nickerson, Larry Coldren, and Jonathan Klamkin are with the Department of Electrical and Computer Engineering, University of California, Santa Barbara, CA 93106 USA (e-mail: pverrinder@ucsb.edu; leiwang@ucsb.edu; jfridlander@ucsb.edu; fsang@ece.ucsb.edu; rosborough@ucsb.edu; nickersonm@ece.ucsb.edu; coldren@ece.ucsb.edu; klamkin@ece.ucsb.edu).

Guangning Yang and Mark Stephen are with the NASA Goddard Space Flight Center, Greenbelt, MD 20771 USA (e-mail: guangning.yang-1@nasa.gov; mark.a.stephen@nasa.gov).

Color versions of one or more figures in this article are available at https://doi.org/10.1109/JSTQE.2021.3086074.

Digital Object Identifier 10.1109/JSTQE.2021.3086074

TABLE I
EPITAXIAL LAYERS FOR ACTIVE-PASSIVE INTEGRATION

	Material	Thickness (nm)	Doping (cm^-3)	Index of refraction
Regrowth Layers	GaAs	200	(p) 5e19	3.2727
	$Al_{0.4}GaAs$	800	(p) 7e17	
	$Al_{0.4}GaAs$	200	(p) 5e17	3.2363
	$Al_{0.4}GaAs$	300	(p) 2e17→5e17	
	$Al_{0.2}GaAs$	50	(p) 2e17	3.3563
Selectively removed for passive sections	GaAs	20	(p) 1e17	3.2727
	GaAs	20	UID	
	$GaAsP_{0.1}$	8	UID	3.44
	$In_{0.271}GaAs$	5	UID	3.6
	$GaAsP_{0.1}$	8	UID	3.44
	$In_{0.271}GaAs$	5	UID	3.6
	$GaAsP_{0.1}$	8	UID	3.44
	$In_{0.271}GaAs$	5	UID	3.6
	$GaAsP_{0.1}$	8	UID	3.44
Base Structure	GaAs	90	UID	3.2727
	$Al_{0.2}GaAs$	100	(n) 1e17	3.2563
	$Al_{0.75}GaAs$	1600	(n) 1e18	3.0535
	GaAs	500	(n) 1e18	3.2727
	GaAs	625+/-20 µm	(n) 2-5e18	

provides a path for future PIC development on GaAs and demonstrates that passive optical components can be integrated with active devices without sacrificing the well-known benefits of strained InGaAs/GaAs QW lasers [9].

II. Material Design and Device Fabrication

The PIC platform presented leverages an etch and regrowth process whereby the active QWs are etched selectively to form active and passive regions, and the upper cladding and p-contact are formed in a subsequent regrowth step. Table I presents the details of the epitaxial layers, including the refractive indices used for simulations, with the layers formed during the regrowth step indicated, as well as the layers that were selectively removed to create passive regions. Lattice mismatched $In_xGa_{1-x}As$ QWs are the most common choice for wavelengths between 0.88 μm and 1.1 μm [9], however the high indium (In) content required to reach longer wavelengths introduces significant strain. To maintain an acceptable cumulative strain in the active region of this multi-QW (MQW) design, 5 nm $In_xGa_{1-x}As$ QWs were used with $x = 0.271$, and 8 nm gallium arsenide phosphide ($Ga_{1-x}AsP_x$) barriers were included with $x = 0.1$ (instead of GaAs barriers) to provide strain compensation. This 3 QW active region is surrounded by GaAs separate confinement heterostructure (SCH) layers, and aluminum gallium arsenide (AlGaAs) is used for both the upper and lower cladding layers. Prior to fabrication and regrowth, the photoluminescence (PL) spectrum of the wafer was measured, and the results are presented in Fig. 1 where the peak PL emission wavelength is 1038 nm. The peak near 870 nm is emission from the GaAs substrate.

Fig. 2 shows schematic diagrams illustrating the primary fabrication process steps, along with simulated mode profiles for the active and passive regions for a 3 μm wide rib waveguide. The active QW material was selectively removed, to form passive regions, using inductively coupled plasma reactive ion etching (ICP-RIE) with chlorine (Cl_2) and nitrogen (N_2) gas chemistry.

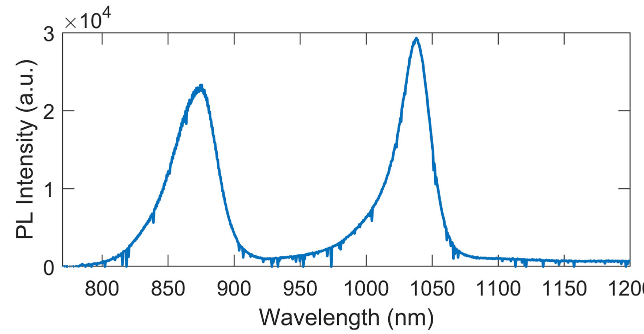

Fig. 1. PL spectrum of epitaxial material prior to fabrication and regrowth.

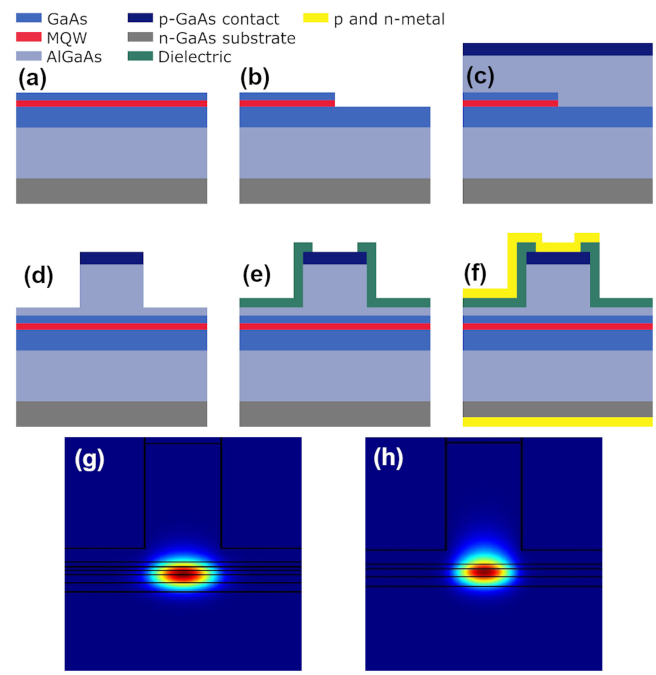

Fig. 2. Summary of primary fabrication steps including (a) initial epitaxial layers, (b) active-passive etch, (c) upper cladding and p-contact layer regrowth, (d) ridge waveguide etch, (e) surface passivation and p-contact via formation, (f) p-metal and n-metal contact formation. Modal simulations for (g) active region and (h) passive region. (a)–(c) are side view illustrations of the active and passive regions. (d)–(f) are cross sections of the active region.

Following regrowth of the upper cladding layer and p-contact layer by metalorganic chemical vapor deposition (MOCVD), the rib waveguides were etched also using a Cl_2/N_2 ICP-RIE process. The etch depth for this step is 1.35 μm, stopping in the upper p-cladding to form a rib waveguide structure as illustrated in Fig. 2(d). The 1.35 μm depth was determined using simulations to optimize QW overlap, active-passive coupling, and eliminate some of the high order transverse modes. This waveguide structure also mitigates scattering loss due to surface roughness by burying the mode below the fabricated ridge. The device was passivated by depositing 100 nm of silicon nitride (SiN) followed by 300 nm of silicon dioxide (SiO_2). This was followed by via formation by etching the dielectric layers to expose the GaAs p-contact layer. Ti/Pt/Au (10/40/1000 nm) was used to form the topside p-contacts, and Ti/Pt/Au (20/40/500 nm) was used for the backside n-contact. The GaAs substrate was thinned to approximately 150 μm before depositing the n-contact metal, and then laser bars were cleaved to form facets and to facilitate characterization. Both all-active and active-passive lasers were fabricated and characterized.

The active-passive platform was designed to enable efficient coupling of light between the active and passive sections, and in turn to minimize reflection at the interface. Figs. 2(g) and 2(h) show the simulated mode profile in the active and passive regions for a 3 μm wide rib. The overlap integral of these mode profiles was calculated to determine that 96% of the optical power in the fundamental TE mode is coupled directly between the active and passive sections. For the fundamental TE mode, the effective index difference between the active and passive waveguides is only 0.0548, and the active-passive interface is angled at 67° with respect to the waveguide propagation direction so that any reflections back into the active region waveguide are minimized. To maximize optical coupling between active and passive regions in the offset QW design, the QWs should be placed near the top of the active layer stack to minimize the height of the "step" illustrated in Fig. 2(b). However, this comes with a tradeoff, as the fractional overlap of the optical mode with the thin QW layers, i.e., the confinement factor Γ_{QW}, should be maximized to allow for sufficient gain in the active region. The design presented in Table I vertically places the QWs in the upper half of the active region, with thinner GaAs and AlGaAs SCH layers above, allowing for efficient active-passive coupling while still achieving an overall confinement factor Γ_{QW} of 5.02% for all three QWs. Considering the large material gain characteristic of the InGaAs QWs, this is sufficient for realizing highly efficient laser operation.

Laser devices were fabricated with varying waveguide widths. These included 2 μm, 2.5 μm, 3 μm, 4 μm, and 5 μm wide all-active Fabry Perot (FP) lasers, and active-passive FP lasers, as well as broad area laser diodes with widths of 10 μm, 20 μm, 50 μm, and 100 μm. Fig. 3 shows a scanning electron microscope (SEM) image of the etched active-passive transition prior to regrowth, a SEM tilted cross-section image of a 3 μm wide fabricated laser facet, and a microscope image of completely fabricated active-passive laser and all-active laser. Figure 3(b) shows both the base epitaxial layers and the upper cladding layer, with no apparent defects or discontinuities at the regrowth interface.

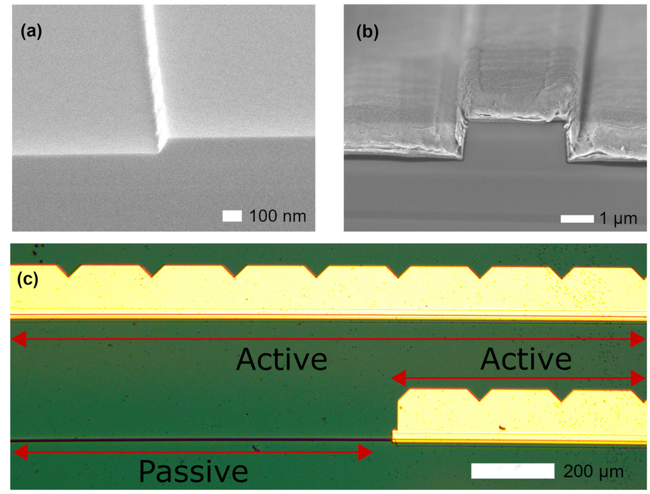

Fig. 3. SEM image of (a) etched active-passive transition prior to regrowth, (b) active side cleaved facet of 3 μm wide fabricated laser, and (c) top view microscope image of completed devices on the processed wafer, showing an all-active FP laser and an active-passive FP laser. The notches in the metal are spaced 200 μm apart and were placed simply as a visual aid for cleaving devices.

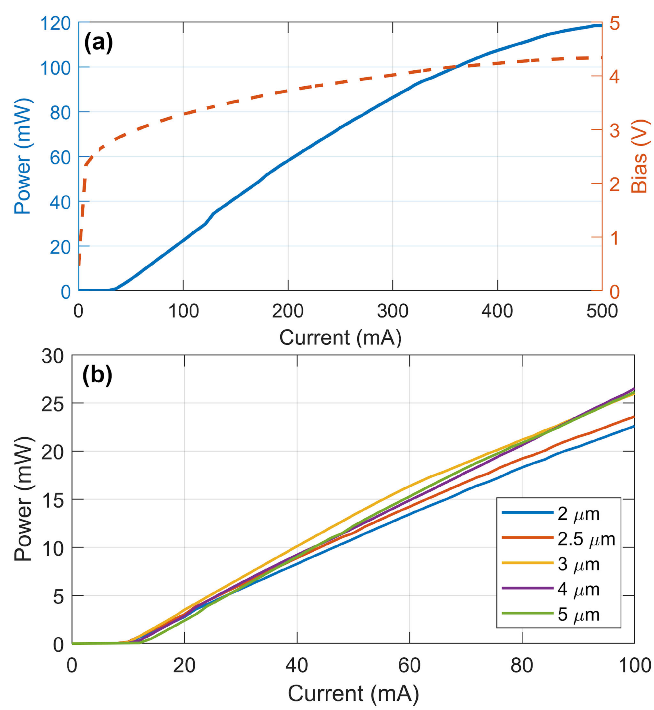

Fig. 4. Light-current characteristics for (a) 20 μm wide by 800 μm long broad area laser and (b) 600 μm long lasers between 2 μm and 5 μm wide under CW current injection.

III. Device Testing and Characterization

To characterize the gain material and the passive waveguides, multiple cleaved-facet FP lasers of various widths and lengths were tested. These devices include all-active lasers and active-passive lasers. Light-current-voltage (LIV) characteristics were measured for the devices under both continuous wave (CW) and pulsed current operation using 500 ns pulse widths at 0.5% duty cycle. Fig. 4(a) shows a typical LIV characteristic measured from one side of a 20 μm wide cleaved facet broad area laser with 800 μm long cavity under CW applied current. This device exhibits 120 mW output power from a single side (240 mW total) with a peak wall-plug efficiency of 16%, differential efficiency of 57.8% (from both sides), and threshold current of 35.2 mA. Additional measurements on a 20 μm wide laser with a 2 mm long cavity exhibited threshold current density as low as 94 A/cm^2. Similarly, Fig. 4(b) shows single-sided LI curves for five different 600 μm long FP lasers with widths from 2 μm to 5 μm. These lasers all exhibit threshold current below 12.6 mA with the lowest threshold being 9 mA for the 2.5 μm wide laser. Additionally, the 3 μm, 4 μm, and 5 μm wide devices output

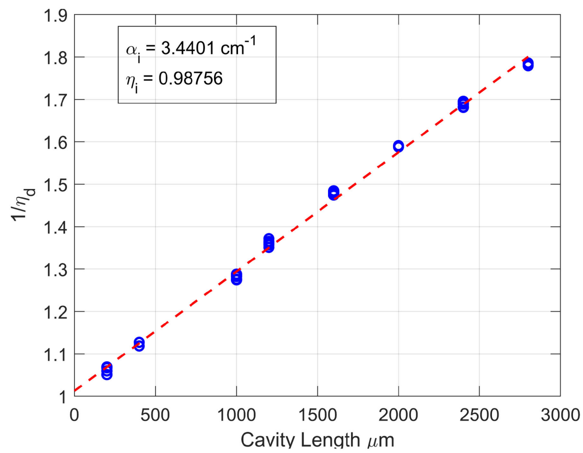

Fig. 5. Inverse differential efficiency as a function of cavity length for 20 μm wide broad area lasers under pulsed current operation with linear fit to extract loss and efficiency.

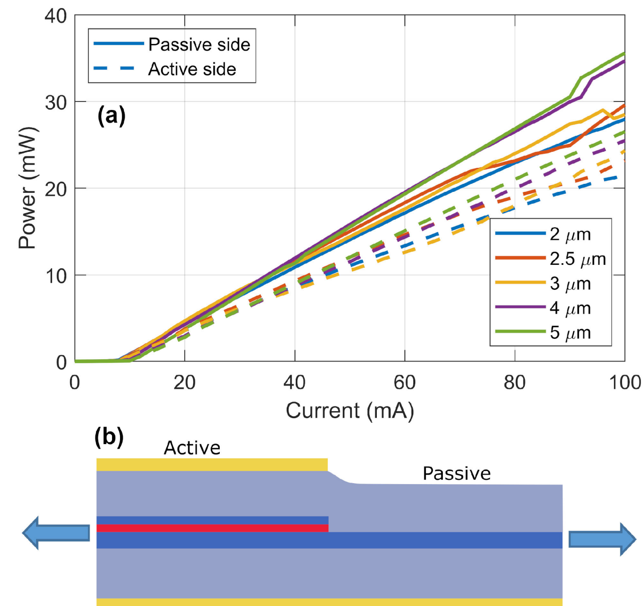

Fig. 6. (a) LI characteristics for active-passive lasers with 400 μm long active section and 400 μm long passive section. (b) Side-view schematic diagram of a generic active-passive laser cavity.

greater than 25 mW of optical power from each facet at 100 mA CW current. The differential efficiencies from both facets are approximately 55% for all three of these laser geometries.

A. Measurement and Extraction of Laser and Material Properties

The internal quantum efficiency, η_i, and internal loss, $\langle\alpha_i\rangle$, were extracted by measuring the differential efficiency, η_d, for multiple device lengths for FP lasers that are otherwise identical. The following relationship was used to extract material parameters:

$$\frac{1}{\eta_d} = \frac{\langle\alpha_i\rangle}{\eta_i \ln\left(\frac{1}{R}\right)} L + \frac{1}{\eta_i}, \tag{1}$$

where R is the total reflection coefficient accounting for both mirrors and L is the length of the laser cavity.

For the 20 μm wide broad area lasers, measurements were performed under pulsed current operation, with 500 ns pulses at 0.5% duty cycle, to mitigate self-heating effects and obtain accurate material parameters. Light-current (LI) characteristics were obtained for devices with lengths of 2800 μm, 2400 μm, 2000 μm, 1600 μm, 1200 μm, 1000 μm, 400 μm, and 200 μm, and the differential efficiency was extracted for each LI curve and plotted as a function of cavity length in Fig. 5. A linear curve fit to (1) was used to extract an η_i of 98.8% and $\langle\alpha_i\rangle$ of 3.44 cm^{-1}. These devices exhibit state of the art performance in terms of efficiency and loss when compared to results from similar devices with strained InGaAs QWs on GaAs [14]–[17].

For comparison to the LI characteristics in Fig. 4(b) for all-active lasers, Fig. 6(a) shows LI characteristics for active-passive FP lasers with various waveguide widths, all with a 400 μm long gain section coupled to a 400 μm long passive section as shown in the schematic of Fig. 6(b), and the device image of Fig. 3(c). The laser optical power was measured from both sides of the devices as reported in Fig. 6(a). The slightly lower power from the active side is to be expected as the active layers create a more reflective cleaved facet mirror due to the slightly higher effective index in this section, and it is the facet reflectivity that determines the fractional power out of each end [18]. The kinks in output power at high current injection are due to mode hopping, as these waveguides are not single transverse mode. Compared to the data for the all-active lasers shown in Fig. 4, the active-passive devices demonstrate comparable performance in terms of power output, differential efficiency, and threshold current. All five of the active-passive lasers measured exhibit threshold currents below 10.7 mA and as low as 7 mA for the 2 μm wide laser. The total output power from both sides was measured to be greater than 50 mW for all devices and as high as 62 mW for the 5 μm wide laser at 100 mA CW current.

Similar to the procedure for extracting $\langle\alpha_i\rangle$, the loss in the passive section can be extracted by obtaining LI measurements for multiple active-passive devices with a constant active section length but varying passive section lengths. For a laser cavity with both active and passive sections, the total differential efficiency from both sides is given by [18]:

$$\eta_{\ d} = \eta_i\ \eta_{da}\eta_{dp}, \tag{2}$$

where,

$$\eta_{da} = \frac{ln\sqrt{\frac{1}{R_1 R_2}}}{\langle\alpha_i\rangle^a_{xy} L_a + ln\sqrt{\frac{1}{R_1 R_2}}}, \tag{3}$$

and

$$\eta_{dp} = \frac{\frac{1-R_1}{\sqrt{R_1}} + \frac{1-R_3}{\sqrt{R_3}}}{\frac{1-R_1}{\sqrt{R_1}} + \frac{1-R_3 e^{-2\alpha_{ip} L_p}}{\sqrt{R_3} e^{-\alpha_{ip} L_p}}}, \tag{4}$$

R_1 is the reflection coefficient at the active-air interface, R_2 is the reflection coefficient at the active-passive interface, R_3 is the reflection coefficient at the passive-air interface, L_a is the

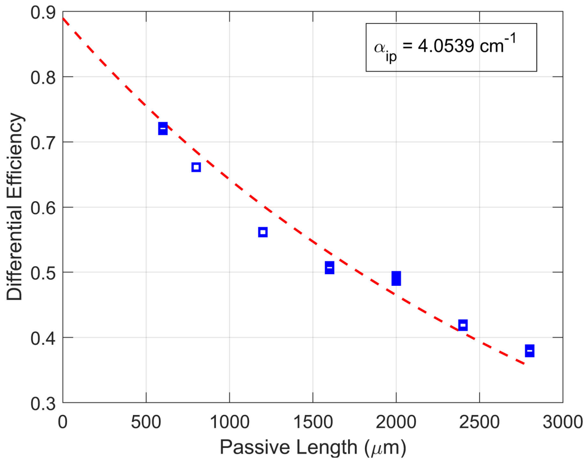

Fig. 7. Differential efficiency as a function of passive section length for 3 μm wide active-passive FP lasers with 400 μm long gain sections.

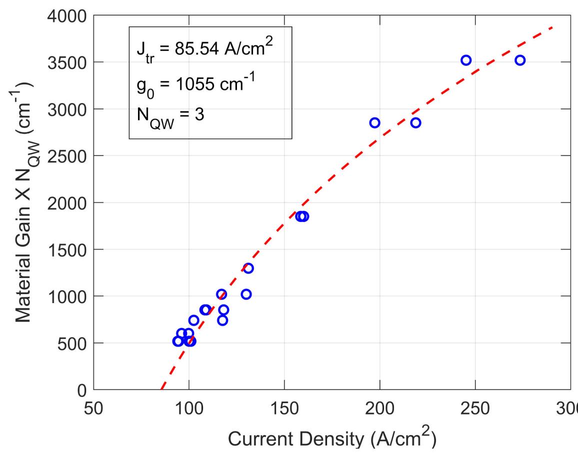

Fig. 8. Material gain as a function of current density for three 5 nm $In_xGa_{1-x}As$ ($x = 0.271$) QWs with 8 nm $Ga_{1-x}AsP_x$ ($x = 0.1$) barriers, obtained from 20 μm wide lasers measured under pulsed current operation.

gain section length, L_p is the passive section length, $\langle \alpha_{ia} \rangle$ is the internal loss in the active region (3.44 cm^{-1} as extracted from all-active lasers), and α_{ip} is the internal loss in the passive region. For the purpose of calculations, R_1, R_2, and R_3 were obtained from simulations as, 0.290, 6.86e-5, and 0.284, respectively.

LI measurements were performed under pulsed current operation for 3 μm wide active-passive FP lasers with a 400 μm long active section length and a passive section that was cleaved back in increments from 2800 μm to 600 μm. Power output was measured from both sides at each length to obtain the total differential efficiency, η_d, for each laser, and these data points were plotted as a function of passive section length as shown in Fig. 7. Combining equations (3) and (4) with equation (2) and using the internal loss and injection efficiency from the all-active laser measurements, α_{ip} is the only unknown quantity and therefore can be extracted. To obtain an accurate value for α_{ip}, a fit to equation (2) was applied to the experimental data points as in Fig. 7. The extracted internal passive loss was 4.05 cm^{-1}.

It may initially seem counterintuitive that the passive waveguide loss is higher than the active internal loss. Although the epitaxial layer structure was originally designed for higher (75%) aluminum (Al) content for the $Al_xGa_{1-x}As$ p-cladding layer, 40% Al was instead used because of the immaturity of the high Al content regrowth. The lower Al content leads to higher refractive index (3.236 at 1030 nm for $Al_xGa_{1-x}As$ with $x = 0.4$), and therefore lower index contrast between the core and cladding. The lower index contrast reduces the optical mode confinement leading to more overlap with the p-doped cladding, leading to additional loss from free-carrier absorption [19]. The Al content for the upper cladding can be increased for future devices and PICs to overcome this issue. Optical mode simulations for a design with 60% Al in the p-cladding show significant improvement in mode confinement, decreasing the amount of overlap with the p-cladding significantly. A calculation of theoretical free-carrier absorption loss [19] indicates that increasing the Al to 60% to improve confinement will decrease the overall passive loss to 3.6 cm^{-1}. Further adjustments, such as increasing the thickness of the GaAs waveguide layer and optimizing the p-doping profile could reduce the passive internal loss further.

The threshold current was also measured for each of the device lengths reported in Fig. 5, and these values were used to calculate each threshold current density. Using the internal loss extracted, the threshold modal gain, Γg_{th}, was also calculated for each length and plotted as a function of current density in Fig. 8. The threshold modal gain is given by:

$$\Gamma\, g_{th} = \alpha_{ia} + \frac{1}{L} \ln\left(\frac{1}{R}\right), \tag{5}$$

where L is the cavity length, and R is the total reflection coefficient. Gain versus current density data can be fitted to an exponential two-parameter curve,

$$J = J_{tr}\, e^{\frac{g}{g_0}}, \tag{6}$$

where J_{tr} is the transparency current density, and g_0 is a fitting parameter. The experimental data points shown in Fig. 8 were fitted to this characteristic curve to extract a transparency current density of 85.54 A/cm^2 and g_0 of 1055 cm^{-1}. These values compare favorably to similar state-of-the-art lasers reported in the literature.

B. Laser Spectral Measurements and Thermal Performance

The light output from a 3 μm wide active-passive laser with 400 μm long active and passive sections (800 μm total length) was coupled to a lensed optical fiber and connected to an optical spectrum analyzer (OSA) to measure the laser output spectrum at different current injection levels. These spectra are shown in Fig. 9. The spectrum is slightly red-shifted compared to the PL emission from Fig. 1, showing a lasing peak near 1045 nm near lasing threshold (8 mA current), compared to the PL emission wavelength of 1038 nm. This is expected because self-heating causes the laser output to shift to longer wavelengths under CW current injection, as observed in Fig. 9. It should also be noted that this waveguide is not a single mode waveguide in

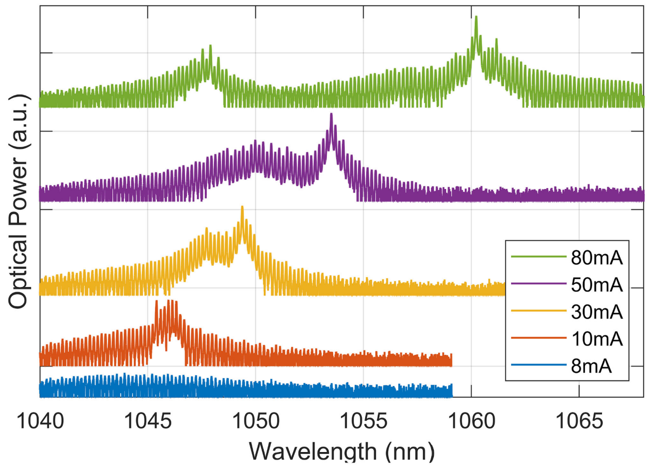

Fig. 9. Lasing spectra for 3 μm wide active-passive laser with 400 μm long gain section and 400 μm long passive section under various levels of CW current injection.

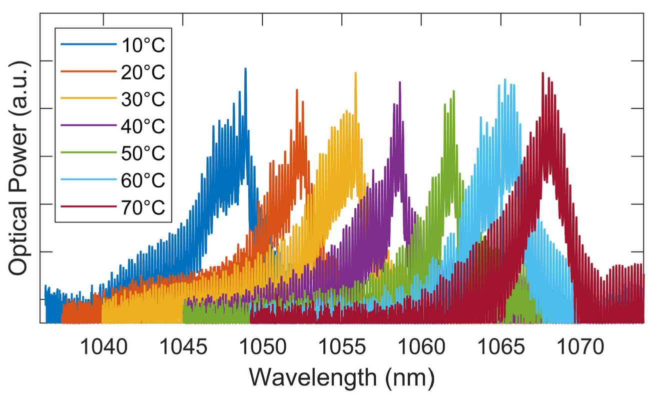

Fig. 10. Lasing spectra for various temperatures for 3 μm devices at 40 mA CW current.

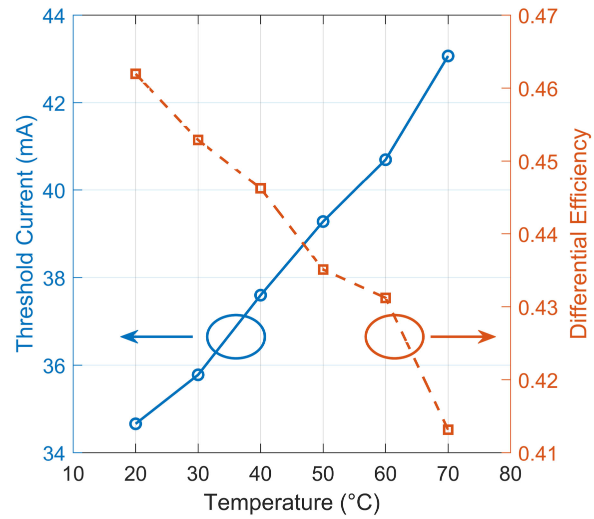

Fig. 11. Threshold current and single-sided differential efficiency as a function of temperature for a 20 μm wide, 400 μm long broad area laser. Measurements were performed with pulsed current to mitigate self-heating, while the stage temperature was varied from 20 °C to 70 °C.

the transverse direction, as evidenced by the two distinct peaks in the lasing spectrum particularly at higher current injection levels. This multi-mode behavior was expected based on simulations, which showed that the 3 μm wide waveguide supports the horizontal TE_1 mode in addition to the fundamental mode. However, this is not a concern since future applications planned for this platform will include grating mirrors that provide some mode filtering.

The effect of heating on the lasing wavelength is observed more directly in Fig. 10 where the same device was characterized under constant CW current injection at 40 mA while the temperature was varied from 10 °C to 70 °C. The peak lasing wavelength shifts predictably to longer wavelengths at a rate of 0.32 nm/°C as the temperature is increased.

Additional measurements were taken to determine thermal characteristics of these devices. Both the threshold current and differential efficiency exhibit an exponential dependence on temperature, with an increase in temperature leading to higher threshold and lower differential efficiency. The relative change in threshold current can be expressed by [18],

$$\frac{I_{th1}}{I_{th2}} = \exp\left(\frac{T_1 - T_2}{T_0}\right), \tag{7}$$

where T_1 and T_2 are the initial and final temperatures, I_{th1} and I_{th2} are initial and final threshold currents, and T_0 is the overall characteristic temperature. LIV measurements were obtained at different temperatures to observe the change in threshold current with heating and to obtain a value for characteristic temperature, resulting in $T_0 = 205$ K, which is consistent with commonly reported values for InGaAs QW lasers on GaAs [14]. Fig. 11 reports the experimentally determined threshold current as a function of temperature for the data points used with (6) to obtain T_0. Similarly, heating also has a deleterious effect on laser efficiency, with greater current required to obtain the same output power at higher temperature. There is a characteristic temperature for differential efficiency, T_η, which can be obtained by calculating the ratio of differential efficiencies at different temperatures,

$$\frac{\eta_{d1}}{\eta_{d2}} = \exp\left(-\frac{T_1 - T_2}{T_\eta}\right). \tag{8}$$

where η_{d1} and η_{d2} are the initial and final differential efficiencies, and T_η is the characteristic temperature. From the same measurements used to calculate T_0, differential efficiency as a function of temperature was also obtained and plotted in Fig. 11, and (7) was used to extract a $T_\eta = 577$ K from the experimental data points. This data was obtained from a 20 μm wide, 400 μm long laser that was tested under pulsed current operation while the temperature was varied with a thermoelectric cooler (TEC).

Both the all-active FP lasers from Fig. 4 and the active-passive FP lasers from Fig. 6 exhibit state-of-the-art performance in terms of threshold current, efficiency, loss, gain characteristics, and temperature dependence when compared to similar devices reported in literature [14]–[17]. This demonstrates that the offset QW design, active-passive etch, and subsequent upper cladding regrowth process presented here offers a suitable platform for active-passive photonic integration without sacrificing the well-known performance advantages of the InGaAs/GaAs material

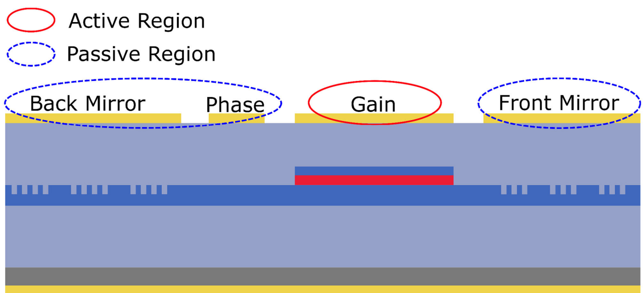

Fig. 12. Schematic diagram of four section SGDBR laser.

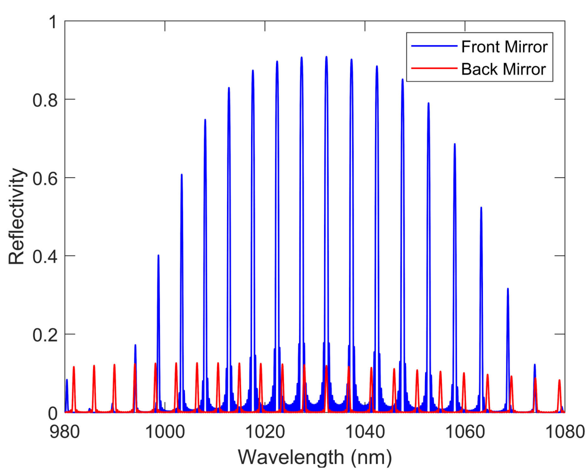

Fig. 13. SGDBR front and back mirror reflectivity spectra.

system for optical gain. This platform is viable for advanced monolithic PICs that incorporate lasers with other active and passive components.

IV. Tunable Laser Design and Development

The platform presented can be used for constructing PICs with integrated single frequency and tunable lasers such as DBR or DFB lasers. To extend the tunable range for topographical Lidar applications, we are pursuing sampled grating DBR (SGDBR) laser designs [20]. Fig. 12 shows a side-view schematic of a generic SGDBR laser that includes a gain section, phase section, and front and back SGDBR mirrors. These devices can optionally include a semiconductor optical amplifier (SOA) that follows the front mirror for amplification. Such a PIC tunable laser can be realized with our nominal 1030 nm active-passive integration technique.

The viability of this platform for active-passive integration has already been demonstrated with the FP laser results presented. With some modifications to the regrowth layers for performance improvement, the only additional step required for a tunable SGDBR laser such as that illustrated in Fig. 12 is the formation of the grating mirrors. Initial development has been carried out, and Fig. 13 shows a simulation of front and back mirror reflectivity spectra for a tunable SGDBR laser design. The grating etch depth is 35 nm resulting in a coupling coefficient for the unsampled gratings of $\kappa = 486$ cm^{-1}, calculated from the effective index

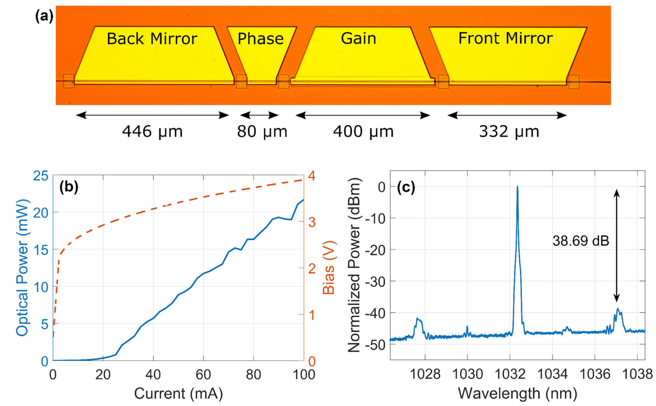

Fig. 14. (a) Top view microscope image of SGDBR laser, (b) LIV curve and (c) free running laser output spectrum.

difference of the simulated mode in the etched and unetched regions of the grating for a 3 μm wide waveguide. This mirror design is expected to tune over a range of at least 23 nm, and possibly as much as 30 nm depending on the effective index change that can be achieved via current injection.

Gratings were patterned with electron beam lithography (EBL). The grating pitch is 157 nm with a 50% duty cycle for a Bragg wavelength at 1032.5 nm. The gratings were etched using ICP-RIE and the same regrowth procedure developed for the active-passive lasers was utilized to overgrow the gratings and form the p-cladding in both the active and passive sections. Fig. 14(a) shows a top-view microscope image of a fabricated SGDBR laser like that shown schematically in Fig. 12. Figures 14(b) and (c) show the LIV curve and free running output spectrum, respectively, from a laser fabricated with these gratings. This result is preliminary, and further fabrication and characterization is being carried out in pursuit of widely tunable lasers, however this demonstrates that the active-passive integration process presented here is feasible for lasers with grating mirrors.

To the best of the authors knowledge, this would be the first realization of in-plane extended tuning range lasers on GaAs centered around 1030 nm and would provide a viable path toward widely tunable laser PICs for Lidar and other applications requiring low system CSWaP.

V. Conclusion

An active-passive PIC platform on GaAs was demonstrated for operation near 1030 nm. This platform integrates active sections with gain, with passive sections, while maintaining state-of-the-art FP laser performance for this material system. The design and fabrication development for widely tunable lasers that will leverage this platform were also reported. Such a tunable laser PIC platform is valuable for airborne Lidar applications that require low system CSWaP for deployment on small platforms. Future work will include modification of the upper cladding regrowth design to decrease the passive section loss; by increasing the Al content in the p-cladding to 60%, which will decrease the refractive index of this layer, the optical mode will be more confined in the waveguide core layers thus decreasing free-carrier absorption loss due to the modal overlap with the p-doped cladding. By etching the tunable laser gratings following the active-passive etch, the same regrowth process can be leveraged to simultaneously overgrow the gratings and form the upper cladding for the active and passive sections. This fairly elegant active-passive platform can therefore realize highly complex PICs for applications with an operating wavelength near 1030 nm.

REFERENCES

[1] F. Kish *et al.*, "From visible light-emitting diodes to large-scale iii-v photonic integrated circuits," *Proc. IEEE*, vol. 101, no. 10, pp 2255–2270, Oct. 2013

[2] J. Klamkin *et al.*, "Indium phosphide photonic integrated circuits: technology and applications," in *Proc. IEEE BiCMOS Compound Semicond. Integr. Circuits Technol. Symp.*, San Diego, CA, USA, 2018, pp. 8–13, doi: 10.1109/BCICTS.2018.8550947.

[3] F. A. Kish *et al.*, "Current status of large-scale InP photonic integrated circuits," *IEEE J. Sel. Topics Quantum Electron.*, vol. 17, no. 6, pp. 1470–1489, Nov./Dec. 2011, doi: 10.1109/JSTQE.2011.2114873.

[4] B. J. Isaac, B. Song, S. Pinna, L. A. Coldren, and J. Klamkin, "Indium phosphide photonic integrated circuit transceiver for FMCW LiDAR," *IEEE J. Sel. Topics Quantum Electron.*, vol. 25, no. 6, pp. 1–7, Nov./Dec. 2019, doi: 10.1109/JSTQE.2019.2911420.

[5] J. Fridlander *et al.*, "Photonic integrated circuits for precision spectroscopy," in *Proc. Conf. Lasers Electro-Opt.*, 2020.

[6] H. Zhao *et al.*, "Indium phosphide photonic integrated circuits for free space optical links," *IEEE J. Sel. Topics Quantum Electron.*, vol. 24, no. 6, pp. 1–6, Nov./Dec. 2018, doi: 10.1109/JSTQE.2018.2866677.

[7] M. A. Krainak, X. Sun, G. Yang, and W. Lu, "Comparison of linear-mode avalanche photodiode lidar receivers for use at one-micron wavelength," in *Proc. SPIE Defense, Secur., Sens.,* Orlando, FL, USA, 2010, pp. 76810Y-1–76810Y-13.

[8] A. W. Yu *et al.*, "A 16-beam non-scanning swath mapping laser altimeter instrument" in *Proc. SPIE LASE,* San Francisco, CA, USA, 2013, pp. 85990P-1–85990P-15.

[9] J. J. Coleman, "Strained-layer InGaAs quantum-well," *IEEE J. Seel. Topics Quantum Electron.,* vol. 6, no. 6, pp. 1008–1013, Nov./Dec. 2000.

[10] A. Pietrzak, M. Zorn, R. Huelsewede, J. Meusel, and J. Sebastian, "Development of highly-efficient laser diodes emitting around 1060nm for medical and industrial applications," in *Proc. SPIE LASE*, San Francisco, CA, USA, 2019, pp. 1009000K-1–100900K-9.

[11] W. Gao *et al.*, "High-power 1060-nm InGaAs/GaAs single-mode laser diodes," in *Proc. SPIE LASE,* San Jose, CA, USA, 2005, pp. 58–65.

[12] S. Spieberger *et al.*, "DBR laser diodes emitting near 1064 nm with a narrow intrinsic linewidth of 2 kHz," *Appl. Phys. B Lasers Opt.*, vol. 104, no. 4, pp. 813–818, 2011, doi: 10.1007/s00340-011-4644-7.

[13] H. Wenzel, J. Fricke, A. Klehr, A. Knauer, and G. Erbert, "High-power 980-nm DFB RW lasers with a narrow vertical far field," *IEEE Photon. Technol. Lett.*, vol. 18, no. 6, pp. 737–739, Mar. 2006, doi: 10.1109/LPT.2006.871127.

[14] Z. Qiao *et al.*, "High-performance 1.06-μm InGaAs/GaAs double-quantum-well semiconductor lasers with asymmetric heterostructure layers," *Semicond. Sci. Technol.*, vol. 34, no. 5, 2019, doi: 10.1088/1361-6641/ab110b.

[15] X. Li, L. H. Duan, Y. Zhou, A. P. Liu, and Z. R. Wei, "Strained InGaAs/GaAs quantum-well laser emitting at 1054 nm," *J. Supercond. Nov. Magn.*, vol. 23, no. 6, pp. 937–939, 2010, doi: 10.1007/s10948-010-0741-9.

[16] S. Y. Hu, D. B. Young, S. W. Corzine, A.C. Gossard, and L. A. Coldren, "High-efficiency and low-threshold InGaAs/AlGaAs quantum-well lasers", *J. Appl. Phys.,* vol. 76, no. 6, pp. 3932–3934, 1994

[17] N. Tansu and L. J. Mawst, "High-performance strain-compensated InGaAs-GaAsP-GaAs (λ = 1.17 μm) Quantum-Well Diode Lasers," *IEEE Photon. Technol. Lett.,* vol. 13, no. 3, pp. 179–181, Mar. 2001.

[18] L. A. Coldren, *Diode Lasers and Photonic Integrated Circuits,* 2nd ed. Hoboken, NJ, USA: Wiley, 2012.

[19] K. A. Bulashevich, V. F. Mymrin, S. Y. Karpov, D. M. Demidov, and A. L. Ter-Martirosyan, "Effect of free-carrier absorption on performance of 808 nm AlGaAs-based high-power laser diodes," *Semicond. Sci. Technol.*, vol. 22, no. 5, pp. 502–510, 2007, doi: 10.1088/0268-1242/22/5/008.

[20] V. Jayaraman, Z. M. Chuang, and L. A. Coldren, "Theory, design, and performance of extended tuning range semiconductor lasers with sampled gratings," *IEEE J. Quantum Electron.*, vol. 29, no. 6, pp. 1824–1834, Jun. 1993, doi: 10.1109/3.234440.

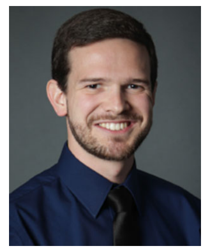

Paul A. Verrinder received the B.S. degree in electrical engineering from California State University, Fresno, Fresno, CA, USA, in 2015, and the M.S. degree in electrical and computer engineering from the University of California, Santa Barbara (UCSB), Santa Barbara, CA, USA, in 2020. He is currently working toward the Ph.D. degree with Electrical and Computer Engineering Department, UCSB. From 2015 to 2018, he was an Electrical Engineer with NAVAIR, China Lake, China. His research interests include integrated photonics for optical communications and LIDAR.

Lei Wang received the B.S. degree in physics from Shandong University, Jinan, China in 2014 and the M.S. degree in electrical and computer engineering from the University of California, Santa Barbara (UCSB), Santa Barbara, CA, USA, in 2019. He is currently toward the Ph.D. graduate degree with Electrical and Computer Engineering Department, UCSB. From 2014 to 2017, he was a Project Research Assistant affiliated by Shandong University and the Institute of Semiconductors, Chinese Academy of Sciences, Beijing, China. His research interests include quantum dot lasers and silicon photonics.

Joseph Fridlander received the B.S. and M.Eng. degrees in electrical and computer engineering from Cornell University, Ithaca, NY, USA, in 2012 and 2013, respectively. He is currently working toward the Ph.D. degree as a Member of Integrated Photonics Laboratory, UCSB. From 2013 to 2016, he was an RF Microwave Engineer with Jet Propulsion Laboratory, La Cañada Flintridge, CA, USA, where he developed ground system communications for NASA's Deep Space Network. His current research interests include photonic integrated circuits for free space optical communications and LIDAR remote sensing instruments.

Fengqiao Sang received the B.S. degree from Drexel University, Philadelphia, PA, USA and the M.S. degree from the University of California, Santa Barbara, Santa Barbara, CA, USA, where he is currently working toward the Ph.D. degree. His research interests include semiconductor photonic integrated circuits and integrated LIDAR.

Victoria Rosborough received the B.S. degree in physics from Mary Baldwin University, Staunton, VA, USA, in 2012 and the M.S. degree in applied physics from the University of Oregon, Eugene, OR, USA, in 2013. She is currently working toward the Ph.D. degree with Integrated Photonics Lab, Department of Electrical and Computer Engineering, University of California Santa Barbara, Santa Barbara, CA, USA. Her research focuses on semiconductor photonic integrated circuits for free space communications and sensing.

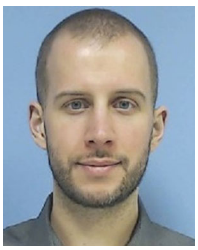

Michael Nickerson received the bachelor's degree in physics from the University of Washington, Seattle, WA, USA. He is currently working toward the Ph.D. degree with Electrical and Computer Engineering Department, University of California Santa Barbara, Santa Barbara, CA, USA. After the bachelor's degree, he was with JILA, Boulder, CO, USA and with MIT Lincoln Laboratory, Lexington, MA, USA, for several years. His interests include integrated photonics for free-space optical communications and optical phased arrays**.**

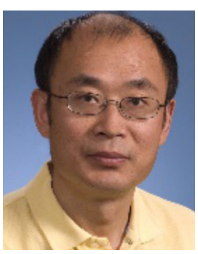

Guangning Yang received the B.S. degree in physics from Sichuan University, Chengdu, China and the Ph.D. degree in electrical engineering from Drexel University, Philadelphia, PA, USA. He was with Tyco Submarine Systems as Lead Design Engineer for the first 10GBPS transmitter for trans-oceanic optical communication. In 2000, he was the Technical Section Lead for high speed optical communication terminal for dorsal or corvis networks. Since 2008, He has been with NASA Goddard Space Flight Center, working on LIDAR and laser ranging and communication. He was the Product Development Lead of photon counting detector for the ATLAS laser altimeter instrument on ICESAT-2 Mission. He is currently working on next generation space LIDAR altimeter and optimetrics experiment on laser communications relay demonstration.

Mark Stephen was born in USA in 1970. He received the B.S. degree in physics from the University of Delaware, Newark, DE, USA, in 1992, and the M.S. and Ph.D. degrees in applied physics from the University of Maryland, Baltimore County, Baltimore, MD, USA, in 2003 and 2008, respectively.

Since 1991, he has been with NASA's Goddard Space Flight Center developing laser and electro-optics technologies for space-based applications. His research interests include lasers, optical components, and laser instruments. He developed diode-pumped solid-state laser systems with an emphasis on laser diode array pumps and the space-qualification of these components, the use of fiber amplifier technology for gas detection and remote sensing using laser spectroscopy and new laser architectures including waveguides. He leads the development of a fiber-based laser transmitter system to measure carbon dioxide in the Earth's atmosphere. He worked on several satellite programs, including the Geoscience Laser Altimeter System, the Mercury Laser Altimeter, and the Lunar Orbiter Laser Altimeter. He was the product development lead for the Advanced Technology Laser Altimeter System Laser, which is currently flying aboard ICESat-2. He is currently working on photonic integrated circuits and mapping LIDARs for space applications.

Larry A. Coldren (Life Fellow, IEEE) received the B.S. degree in electrical engineering and the B.A. degree in physics from Bucknell University, Lewisburg, PA, USA, the M.S. and Ph.D. degrees in electrical engineering from Stanford University, Stanford, CA, USA, in 1969 and 1972, respectively, supported by Bell Lab's. In 1968, he joined Bell Laboratories. Following 13 years in the research area with Bell Laboratories, he joined the ECE Department, University of California at Santa Barbara (UCSB), Santa Barbara, CA, USA, in 1984. In 1986, he was a founding Member of Materials Department. In 1999, he became the Fred Kavli Professor of optoelectronics and sensors. From 2009 to 2011, he was the Dean of the College of Engineering, and in 2017 he became Professor Emeritus and a Distinguished Research Professor.

In 1990, he cofounded optical concepts, later acquired as gore photonics, to develop novel VCSEL technology, and, in 1998, he cofounded agility communications, later acquired by JDSU (currently Lumentum), to develop widely-tunable integrated transmitters and transponders. He has worked on multiple-section widely-tunable lasers and efficient vertical-cavity surface-emitting lasers (VCSELs) with UCSB. He has authored or coauthored more than a thousand journal and conference papers, eight book chapters, a widely-used textbook, and 63 issued patents. He continues to research high-performance InP-based photonic integrated circuits and high-speed, high-efficiency VCSELs for various applications.

He is a fellow of OSA and IEE, and the National Academy of Inventors and a Member of the National Academy of Engineering. He was the recipient of the 2004 John Tyndall, the 2009 Aron Kressel, the 2014 David Sarnoff, the 2015 IPRM, and the 2017 Nick Holonyak, Jr. Awards.

Jonathan Klamkin (Senior Member, IEEE) received the B.S. degree from Cornell University, Ithaca, NY, USA, and the M.S. and Ph.D. degrees from the University of California Santa Barbara (UCSB), Santa Barbara, CA, USA. From 2008 to 2011, he was a Member of the Technical Staff in the Electro-Optical Materials and Devices Group, MIT Lincoln Laboratory, Lexington, MA, USA. From 2011 to 2013, he was an Assistant Professor with the Institute of Communication, Information and Perception Technologies, Scuola Superiore Sant'Anna, Pisa, Italy. From 2013 to 2015, he was an Assistant Professor of electrical and computer engineering (ECE) and materials with Boston University, Boston, MA, USA. In 2015, he joined the ECE Department, University of California Santa Barbara, where he is currently a Professor and the Director of the UCSB Nanotech. He has authored or coauthored 200 journal and conference papers. He or his group members were the recipient of Best Paper awards at the 2006 Conference on Optoelec-tronic and Microelectronic Materials and Devices, 2007 Microwave Photonics Conference, and 2017 and 2019 Asia Communications and Photonics Conference. He was the recipient of the NASA Early Career Faculty Award, the DARPA Young Faculty Award, and the DARPA Director's Fellowship.